Weierstraß-Institut
für Angewandte Analysis und Stochastik

im Forschungsverbund Berlin e.V.

Preprint ISSN 0946 – 8633

Two- and three-dimensional transient melt-flow simulation in vapour-pressure-controlled Czochralski crystal growth

E. Bänsch[1], D. Davis[1], H. Langmach[1],

G. Reinhardt[1], M. Uhle [1]

submitted: 2nd June 2003

[1] Weierstrass Institute for Applied Analysis and Stochastics,
Mohrenstraße 39, D - 10117 Berlin, Germany
E-Mail:
baensch@wias-berlin.de davis@wias-berlin.de langmach@wias-berlin.de
reinhard@wias-berlin.de uhle@wias-berlin.de

No. 852
Berlin 2003

2000 *Mathematics Subject Classification.* 35Q30, 65M60, 76-04, 76D05.

Key words and phrases. axisymmetric, buoyancy, Czochralski, crystal growth, finite-element, GaAs, Navier–Stokes equations, vapour-pressure controlled .

Edited by
Weierstraß-Institut für Angewandte Analysis und Stochastik (WIAS)
Mohrenstraße 39
D — 10117 Berlin
Germany

Fax: + 49 30 2044975
E-Mail: preprint@wias-berlin.de
World Wide Web: http://www.wias-berlin.de/

Abstract

Flow and thermal properties associated with semiconductor melt flow in an axisymmetric crucible container are studied numerically. Axisymmetric and three-dimensional computational solutions are obtained using a standard-Galerkin, finite-element solver. The crucible and crystal are optionally rotated, and the influence of gravity (through buoyancy) is accounted for via a Boussinesq approximation in the controlling Navier-Stokes equations. The results indicate a strong dependence of the flow on both rotation and buoyancy. Results for axisymmetric flows, computed in both flat and curved geometries, are presented first, and strongly suggest that rotation of crystal and crucible in the same direction (iso-rotation) is most favourable for producing a desired convexity for the crystal/melt interface. Three-dimensional results are then presented for higher Reynolds numbers, and, in particular, reveal that for iso-rotation under moderate buoyancy, the flow undergoes a switch from a steady, 2D state to an unsteady 3D state, and that the temperature becomes non-trivially advected by the flow beneath the crystal. Further evidence reveals however, that on a time scale more appropriate to the crystal growth process, the (time-averaged) flow has a weaker three-dimensionality, in relation to its axisymmetric mode, and there is only slight distortion to the temperature field beneath the crystal.

1 Introduction

Semiconductor crystals and their properties are of central importance in the fields of computer technology and communication. An important application is the production of large crystals with homogeneous and low defect concentration. A recently-introduced processing technique for this purpose is the vapour-pressure-controlled Czochralski (VCz) method, which was developed at the Institute for Crystal Growth (IKZ) in Berlin, Germany (Rudolph et al 1997, Rudolph & Jurich 1999, Rehse et al 2001, Miller & Rehse 2001). It is principally used in the growth of gallium arsenide (GaAs) crystals. This method is a variant of the so-called liquid encapsulated Czochralski (LEC) method, wherein melt-free surfaces are covered by a layer of viscous liquid (boron oxide), whose main purpose is to quell excessive heat loss and evaporation of As from the melt. Due to its small thermal conductivity however, it can produce high temperature gradients in the growing crystal, which therefore increases its thermal stress; in the VCz method, this is rectified to some degree, by placing the crystal, melt and encapsulant in an insulated inner chamber. Subsequent temperature-gradient reductions however can lead to a reduction of the crystal quality, owing to sublimation from the hot crystal surface. To combat this, an As source feeds arsenide into the chamber, and thereby establishes a thermodynamical equilibrium in the growing environment.

An important aspect of crystal growth is to choose the proper growth conditions so that the crystal/melt interface assumes a desired shape – for GaAs it is generally considered most desirable to have an interface with a slightly convex (outer) shape, which enables the crystal radius to be maintained at a nearly constant value, as well as ensuring that any dislocations grow outwards. Since the crystallisation front is identified by the melting temperature of the semiconductor, the thermal and hydrodynamic properties of the melt clearly play important rôles. These can be artifically induced in part, by rotating the crystal and crucible, either in the same direction (iso-rotation) or in opposite directions (counter-rotation); alternatively, one or other of the bodies can be rotated. The relative angular velocity of the crystal and crucible, and the relative sizes of the rotation and the naturally-occurring buoyancy, would appear to be important factors on the flow and thermal behaviour in the melt zone, and hence, by implication, on the crystallisation front development itself. In Rehse et al (2001), it was found that, for sufficiently strong forcing (such that the temperature is significantly influenced by the hydrodynamic field), zero rotation (pure buoyancy) and counter-rotation tend to produce ‘wiggly’ (undulating) interfaces, whereas iso-rotation can produce the desired convexity at the interface. The sample of results presented in our work here are wholly consistent with these findings.

The aim of the work here is to gain a better understanding of the melt-flow dynamics and its interplay with associated thermal effects occurring in VCz growth, and the subsequent implications for some crystal properties, notably the crystal/melt interface shape. This is mainly sought through full numerical simulation, with a particular focus on unsteadiness and three-dimensionality. Time-dependent flows are important when some form of thermally induced convection is present, i.e. buoyancy convection and/or Marangoni (thermocapillary) convection, since these effects are known causes for inhomogeneous dopant distribution within the crystal (leading to unwanted striations for the latter form of convection). Although there have been some studies involving three-dimensional simulations of semiconductor melt flow, we remark that these mostly apply to silicon (see e.g. Savolainen et al 2001; Vizman, Friedrich & Müller 2001; Vizman, Gräbner & Müller 2001); however, the prevalence of three-dimensional motion is evident from experimental work (Gräbner et al 2000; Watanabe et al 1995). In the current work, it is assumed that surface-tension variations with temperature are negligible at the fluid-fluid interface of the melt/encapsulant layer, and hence only buoyancy convection is considered in this context. Another simplification here is the absence of latent heat effects at the crystal/melt interface, although we remark here (and in Section 5 below) that a suitable phase-transition model could later be incorporated in our mathematical system in a relatively straightforward manner, without affecting the validity and effectiveness of our current numerical scheme, apart from the likely requirement of locally fine meshes near the interface. Moreover, there is assumed to be no dynamical interaction between the melt and encapsulant (typically boron oxide) fluids, so that we can regard our melt-zone model as closed. In this study, Dirichlet conditions for velocity, based on the rotational speeds and directions of the crystal and crucible alone, are applied at the melt/encapsulant boundary. This choice contrasts with other models, where tangential stress conditions have been applied, either in closed form (Miller, Rehse & Böttcher 1999; Savolainen et al 2001) or as a continuity condition between the melt and encapsulant flows (Fontaine & Randriamampianina 1989; Fontaine et al 1989; Fontaine, Randriamampianina & Bontoux 1991) but is a convenient condition to use in this first, simplified model. We furthermore assume that all interfaces are time-independent. The validity of the assumption for the crystal/melt interface, is partly dependent on the relative timescales controlling the melt motion and the crystal growth itself; however, in practice, the latter is typically $O(10^4)$ – $O(10^5)$ larger, so that any crystal movement would be unnoticeable over the former timescale. This feature also infers that the *time-averaged* flow properties are a more appropriate means of assessing the distortions in the temperature field around the crystallisation front. Hence, time-averaged results are also presented, where appropriate.

In Section 2 we present a brief formulation of the problem, followed by the controlling system of equations acting in the melt flow, along with boundary and initial conditions. Important flow parameters are identified. The finite-element numerical scheme that we adopt to solve the system of equations (in variational form) is then addressed in Section 3, where details of a benchmark test case, used to validate our code, are also included. In Section 4, we present a selection of our numerical results. To illustrate some fundamental flow and thermal mechanisms, we consider the rôle of increasing rotation rate (Reynolds number) on the hydrodynamic/thermal development, for fixed values of the controlling parameters. Also, we restrict our discussion mainly to those cases with equal rotation magnitudes for crystal and crucible, and mostly for iso-rotation. A critical Reynolds number is evident from the numerical results, and the computations indicate that the flow switches from a steady, axisymmetric state to an unsteady three-dimensional one. Some explanation is offered for the phenomena found, as well as the subsequent impact on the crystal/melt interface profile. Finally in Section 5 the conclusions, followed by some further comments, including a brief discussion on extending the present model, are given.

2 The governing system of equations for the melt

We consider a finite volume V of liquid melt contained in an axisymmetric crucible, whose axis is aligned to the direction of gravity ($\hat{\mathbf{e}}_g$). We further suppose that the liquid is incompressible, with kinematic viscosity ν, thermal diffusivity κ and density ρ. We consider for the moment the crucible to be cylindrical in form (but see Section 4.2 below for crucibles with curved bases). We assume a radius of R_c and a height ΛR_c, where Λ denotes the aspect ratio of the cylinder. All melt-zone interfaces are assumed to be planar, with the crystal-melt interface comprising a circular disc of radius $r_X R_c$ ($0 < r_x < 1$). (See Figure 1.)

Natural motion in the melt is induced through buoyancy effects, essentially acting vertically within the melt zone and stemming from the heating of the crucible. Buoyancy here is accounted for in the augmented version of the incompressible Navier–Stokes equations (where an additional Boussinesq forcing occurs), which together with the equations of mass conservation and heat transport (plus the relevant initial and boundary conditions) govern the melt-flow dynamics here. The linearised approximation in the Boussinesq term is valid provided $\delta T/T_X \ll 1$, where $\delta T := T_C - T_X (> 0)$, and T_C, T_X are representative temperatures on the crucible and crystal/melt interface, in turn. An optional further contribution to the melt dynamics stems from rotating the crucible and/or crystal with respective angular speeds Ω_C, Ω_X. The rotation is responsible for a centrifugal effect in the domain, which draws motion towards the outer boundary of the crucible.

The scalings $R_C, U, R_C/U$, ρU^2 and δT are used to non-dimensionalise the length, velocity, time, pressure and temperature deviation from T_X, respectively, and lead to the following form for the governing equations

$$\frac{\partial \mathbf{u}}{\partial t} + (\mathbf{u}\cdot\nabla)\mathbf{u} - \frac{1}{Re}\Delta \mathbf{u} + \nabla p - \frac{Gr}{Re^2} T \hat{\mathbf{e}}_z = \mathbf{0} \quad \text{in} \quad V, \tag{2.1a}$$

$$\nabla \cdot \mathbf{u} = 0 \quad \text{in} \quad V, \tag{2.1b}$$

$$\frac{\partial T}{\partial t} + (\mathbf{u}\cdot\nabla)T - \frac{1}{Re\, Pr}\Delta T = 0 \quad \text{in} \quad V, \tag{2.1c}$$

where $\hat{\mathbf{e}}_\mathbf{z} = -\, \hat{\mathbf{e}}_\mathbf{g}$, $Re \equiv U R_C/\nu$ and U is defined according to the application: in the case of rotation, we define $U \equiv \Omega_X R_C$, unless $|\Omega_X| \ll |\Omega_C|$, in which case $U \equiv \Omega_C R_C$ is used; for pure buoyancy forcing, the scaling $U \equiv (\nu/R_c)\sqrt{Gr}$ is adopted. In the rotational case, the corresponding Reynolds numbers (Re) are:

$$Re_X = \frac{\Omega_X R_c^2}{\nu}, \quad Re_C = \frac{\Omega_C R_c^2}{\nu}. \tag{2.2a,b}$$

The other parameters here are the Grashof and Prandtl numbers:

$$Gr = \frac{\beta \delta T g R_c^3}{\nu^2}, \quad Pr = \frac{\nu}{\kappa}, \tag{2.3a,b}$$

where β is the thermal expansion coefficient at constant pressure, and g is the acceleration due to gravity. For the cases involving some form of rotation it is convenient to use the corresponding thermal Rossby numbers:

$$Ro_X = \frac{Gr}{Re_X^2}, \quad Ro_C = \frac{Gr}{Re_C^2}. \tag{2.4a,b}$$

Here $\mathbf{u}$, p and T denote the dimensionless velocity, pressure and temperature fields, respectively, while V represents the dimensionless cavity.

Next we need to choose boundary conditions appropriate to the model. Firstly, no-slip velocity conditions are applied to the solid boundaries Γ_X and Γ_C, while on the melt/encapsulant layer, we make the assumption that the *angular* velocity is a linear function of radius. For the temperature, we assume this interface is adiabatic, and apply constant-valued Dirichlet conditions on the solid parts. Hence, for the given Reynolds number Re, we may write the associated boundary conditions in the following form:

$$\mathbf{u} = \omega_C r \hat{\mathbf{e}}_\theta, \quad T = 1 \quad \text{on} \quad \Gamma_C, \tag{2.5a}$$

$$\mathbf{u} = \omega_B(r) r \hat{\mathbf{e}}_\theta, \quad \frac{\partial T}{\partial n} = 0 \quad \text{on} \quad \Gamma_B, \tag{2.5b}$$

$$\mathbf{u} = \omega_X r \hat{\mathbf{e}}_\theta, \quad T = 0 \quad \text{on} \quad \Gamma_X, \tag{2.5c}$$

where $\omega_C := Re_C/Re$, $\omega_X := Re_X/Re$ and $\omega_B := \omega_C + (\omega_X - \omega_C)(1-r)/(1-r_X)$ denote the dimensionless angular speeds on Γ_C, Γ_X, Γ_B, in turn, and n denotes the outer normal to the boundary part. For an explanation of other notation please refer to Figure 1.

In the numerical examples of Section 4, the choice $Re = Re_X$ is used throughout (except for the pure buoyancy cases, for which $Re = \sqrt{Gr}$), and in this case $\omega_C = \Omega_C/\Omega_X$ and $\omega_X = 1$.

Finally, initial conditions

$$\mathbf{u} = \mathbf{u}_0, \quad T = T_0 \quad \text{in } V \quad \text{at} \quad t = 0 \tag{2.6a,b}$$

are required to close the system.

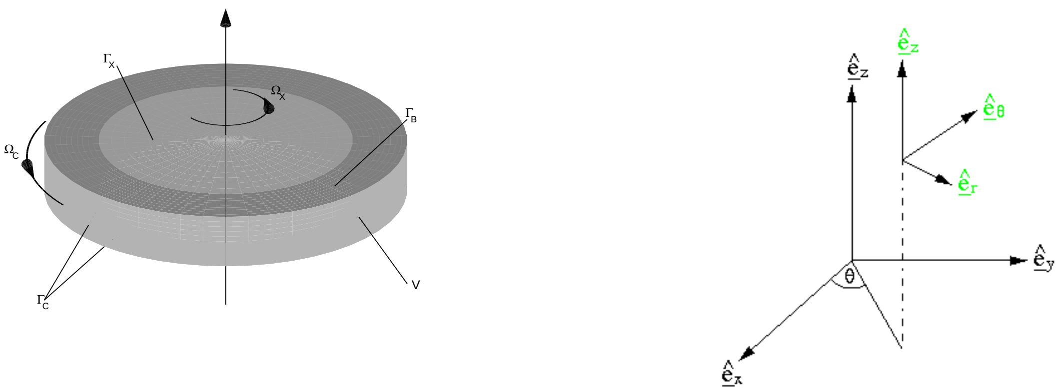

(a)

(b)

Figure 1: (a) Sketch of the semiconductor melt zone (V) in VCz growth, enclosed by the solid-liquid crystal/melt interface Γ_X, the liquid-liquid melt/encapsulant layer Γ_B and the crucible Γ_C. (b) Cylindrical and Cartesian coordinate systems.

3 Numerical Treatment of the Governing Equations

In this section, we summarise the computational method that was applied to the governing system of equations.

3.1 Variational Form and Computational Method

For the spatial discretisation, a standard Bubnov–Galerkin finite-element method was applied to the following variational form of (2.1a-c, 2.5a-c, 2.6a,b):

$$\frac{d}{dt}\int_V \mathbf{u}\cdot\boldsymbol{\phi}\;\,d\mathbf{x} + \frac{1}{Re}\int_V \nabla\mathbf{u} : \nabla\boldsymbol{\phi}\;\,d\mathbf{x} + \int_V [(\mathbf{u}\cdot\nabla)\mathbf{u}]\cdot\boldsymbol{\phi}\;\,d\mathbf{x}$$

$$-\int_V p\nabla\cdot\boldsymbol{\phi}\;\,d\mathbf{x} - \frac{Gr}{Re^2}\int_V T\hat{\mathbf{e}}_z\cdot\boldsymbol{\phi}\;\,d\mathbf{x} = 0, \tag{3.1a}$$

$$\int_V (\nabla\cdot\mathbf{u})\psi\;\,d\mathbf{x} = 0, \tag{3.1b}$$

$$\frac{d}{dt}\int_V T\chi\;\,d\mathbf{x} + \int_V [(\mathbf{u}\cdot\nabla)T]\chi\;\,d\mathbf{x} + \frac{1}{Re\;Pr}\int_V \nabla T\cdot\nabla\chi\;\,d\mathbf{x} = 0, \tag{3.1c}$$

where $\mathbf{u} \in \mathbf{X} := (\mathbf{H}_1(V))^3$, $p \in Y := L_2(V)\setminus\mathbb{R}$, $T \in Z := H_1(V)$, and the test functions $\boldsymbol{\phi}$, ψ, χ are restricted to the spaces $(\mathbf{H}_1^0(V))^3$, Y, $H_1^0(V)$, respectively. Also, we require $\mathbf{u} = \mathbf{u}_0$, and $T = T_0$ at $t = 0$, and note that $\mathbf{u}_0$ should be divergent-free in V and have continuous normal component (zero, for the problem in hand) on all Dirichlet boundary portions (p. 513, Gresho & Sani 2000). Discrete solutions $\mathbf{u_h} \in \mathbf{X}_h$, $p_h \in Y_h$, $T_h \in Z_h$ are sought, such that (3.1a-c) hold for all $\boldsymbol{\phi} \in \mathbf{X}_h^0 := \{\hat{\boldsymbol{\phi}} \in \mathbf{X}_h | \hat{\boldsymbol{\phi}} = \mathbf{0} \text{ on } \delta V\}$, $\psi \in Y_h$, $\chi \in Z_h^0 := \{\hat{\chi} \in Z_h | \hat{\chi} = \mathbf{0} \text{ on } \delta V\}$. Here $\mathbf{X}_h$, Y_h, Z_h are determined by the finite element under consideration. In our applications here, the Taylor–Hood triangular element has been implemented, and hence, the velocity and temperature spaces comprise continuous, piecewise-quadratic polynomials, while continuous, piecewise-linear polynomials form a basis for the discrete pressure space. For this element, the velocity and temperature are of second-order spatial accuracy, while the pressure is of first-order spatial accuracy (in each case, measured relative to $L^2(V)$ norm). For the axisymmetric computations presented here, a slight variation to the form in (3.1a) is used, in that the integrand of the second integral there is replaced with $(D(\mathbf{u}) : D(\boldsymbol{\phi}))/2$, where $D(\mathbf{v}) \equiv \nabla\mathbf{v} + (\nabla\mathbf{v})^{\mathrm{T}}$, is a continuously-differentiable, strain-like tensor; also, an appropriate boundary integral term is added. This form is suitable for accommodating possible stress boundary conditions (which may feature in later models of the problem), as well as for assessing the accuracy of the axisymmetric code via a benchmark problem with such conditions (see Section 3.2 below for details).

To discretise in time, a fractional θ-scheme with operator splitting as variant (Bänsch 1998, Bristeau, Glowinski & Periaux 1987) was applied to the hydrodynamic part coupled with a Crank-Nicolson scheme for the energy equation. To apply the former, the total timestep is first divided into three smaller sub-steps, with the first and third using identical forms of discretisation. In the first and third step, the nonlinear convection term is treated explicitly, but implicitly in the second step; these rôles are exactly reversed for the pressure gradient, while the incompressibility constraint is relaxed in the second step. In both cases the buoyancy term is treated as a source term. The general upshot of this form of discretisation is to produce two distinct types of sub-problem: a self-adjoint, quasi-linear, Stokes system for unknown velocity and pressure; and an asymmetric, nonlinear system for velocity only. As well as full decoupling of the nonlinearity and incompressibility, the fractional θ-scheme is, moreover, virtually non-dissipative and (for self-adjoint operators) unconditionally stable.

In conjunction with the spatial discretisation, the first subproblem reduces to a Schur-complement matrix equation for the pressure together with a positive-definite matrix equation for the velocity. With the former, problems with poor condition number for small time-steps (which are generally unavoidable for larger values of Reynolds number and/or Grashof number, for reasons of accuracy) make it necessary to apply a suitable preconditioner. For this purpose, the method of preconditioning described in Bristeau, Glowinski & Periaux (1987) was employed, and it proved sufficient in obtaining good (iterative) convergence speed and stability, for a wide range of Reynolds and Grashof numbers. Its application essentially leads to two pressure-related, positive-definite, matrix systems, both of which we solved via the method of conjugated gradients; this same method was also used to solve the velocity system. The second subproblem (as well as the fully discretised form of the energy equation) reduces to an asymmetric matrix system for velocity (temperature) only and is solved via the GMRES scheme (Saad & Schulz 1986).

3.2 Benchmark Test Case

As a means of independently validating results obtained via our solver NAVIER, we ran a series of test cases concerned with the numerical simulation of crystal melt flow in a cylindrical crucible and its temperature distribution, as originally proposed by Wheeler (1990).

Referring to the notation introduced in Section 2 above, the test cases have common geometrical properties ($\Lambda = 1; r_X = 0.4$), boundary conditions (see below), and material properties ($Pr = 0.05$) and are distinguishable by the Grashof and Reynolds number values alone. The controlling boundary conditions are:

$$\mathbf{u} = \omega_C r \hat{\mathbf{e}}_\theta, \ \frac{\partial T}{\partial n} = 0 \quad \text{on} \quad \Gamma_{C_1}, \tag{3.2a}$$

$$\mathbf{u} = \omega_C \hat{\mathbf{e}}_\theta, \ T = 1 \quad \text{on} \quad \Gamma_{C_2}, \tag{3.2b}$$

$$\frac{\partial(\mathbf{u}\cdot\hat{\mathbf{e}}_r)}{\partial n} = 0, \ \mathbf{u}\cdot\hat{\mathbf{e}}_z = 0, \ \frac{\partial(\mathbf{u}\cdot\hat{\mathbf{e}}_\theta)}{\partial n} = 0, \ T = \frac{r - r_X}{1 - r_X}, \quad \text{on} \quad \Gamma_B, \tag{3.2c}$$

$$\mathbf{u} = \omega_X r \hat{\mathbf{e}}_\theta, \ T = 0 \quad \text{on} \quad \Gamma_X. \tag{3.2d}$$

A fundamental change to the boundary conditions here, in comparison with (2.5a-c) above, is the application of a free tangential stress condition on the melt/encapsulant layer, as well as a split form for the temperature boundary condition on the crucible: here, we apply a zero-flux condition on the base (Γ_{C_1}), but a constant Dirichlet condition on the cylindrical wall (Γ_{C_2}). Also of note, a Dirichlet condition for temperature, based on linear interpolation, is applied on Γ_B. The liquid mechanics are again controlled by (2.1a-c).

The computational method described in the subsection above was implemented in our calculations, with the exception of the 'stiffness' integral, which used the strain form, described therein. Also, the Taylor–Hood finite element for triangles was used, and our meshes comprised 64×64×2 elements. Our results are summarised in Table 1 below, and include comparisons with those obtained by Bückle & Schäfer (1993), who employed a finite-volume scheme on a regular rectangular grid comprising 64×64 cells; here the comparisons are for the extreme values of the streamfunction, ψ, defined by:

Problem	Parameter			[Bückle/Schäfer(1993)]		NAVIER		Difference
No	Gr	Re_x	Re_c	$\min(\psi_{BS})$	$\max(\psi_{BS})$	$\min(\psi_N)$	$\max(\psi_N)$	d_{rel}
A1	0	10^2	0	-2.3447e-1 $^{1)}$	1.5642e-6	-2.2966e-1	9.8470e-6	2.06e-2
A2	0	10^3	0	-5.3642e+0	1.5257e-4	-5.1492e+0	4.8799e-4	4.01e-2
A3	0	10^4	0	-4.0443e+1	1.9320e-1	-4.2262e+1	1.7701e-1	4.52e-2
B1	0	10^2	-25	-5.0203e-2 $^{2)}$	1.1796e-1	-4.8885e-2	1.1887e-1	1.33e-2
B2	0	10^3	-250	-1.6835e+0	1.2414e+0	-1.5304e+0	1.2158e+0	6.11e-2
B3	0	10^4	-2500	-8.5415e+0	5.2708e+0	-8.6893e+0	5.5183e+0	2.86e-2
C1	10^5	0	0	-1.1936e-3	2.8437e+1	-1.6067e-3	2.8696e+1	9.12e-3
C2	10^6	0	0	-3.9699e-1	9.2100e+1	-2.7504e-1	9.2874e+1	9.69e-3
D1	10^5	10^1	0	-4.7057e-4	2.8420e+1	-1.5614e-3	2.8328e+1	3.28e-3
D2	10^5	10^2	0	-4.7092e-4	2.8393e+1	-1.5617e-3	2.8301e+1	3.28e-3
D3	10^5	10^3	0	-6.5631e-1	2.4829e+1	-6.4850e-1	2.5013e+1	7.53e-3

Table 1: Parameters and results for stationary benchmark test cases defined in Wheeler (1990)

$$\mathbf{u} \cdot \hat{\mathbf{e}}_r = \frac{1}{r}\frac{\partial \psi}{\partial z}, \quad \mathbf{u} \cdot \hat{\mathbf{e}}_z = -\frac{1}{r}\frac{\partial \psi}{\partial r}, \tag{3.2a,b}$$

and subject to:

$$\psi = 0 \quad \text{on the boundary and axis.} \tag{3.2c}$$

In Table 1 we have used the following norm to measure the relative difference between our results and those of Bückle & Schäfer for each case:

$$d_{rel} = \frac{|\max(\psi_N) - \max(\psi_{BS})| + |\min(\psi_N) - \min(\psi_{BS})|}{|\max(\psi_{BS})| + |\min(\psi_{BS})|} \tag{3.3}$$

Table 1 generally reveals very good agreement between the two sets of results, especially for the problem classes C and D, where the difference in each case is less than 1%; the larger differences (up to just over 6% for case B2) occur for the problem classes A and B, which involve some form of rotation and zero buoyancy convection, but even these are relatively small and, in the given context, acceptable, we feel. We have assumed that two of the Bückle & Schäfer entries (superscripted '1)' and '2)' in Table 1) were originally misprinted in the authors' paper, where the exponents were quoted as 1 and -1, respectively. This belief is strongly supported by circumstantial evidence, specifically the close agreement for more extreme parameter values within the classes A and B. We remark further, that the Bückle & Schäfer results were also used by Bärwolff (1995), to help validate his finite-volume solver, and again close agreement was obtained.

4 Numerical results

Here we present a cross-section of our results to date, starting with axisymmetric computations in both flat- and curved-based crucibles, and followed by 3D computations in a flat-based crucible only. We mainly focus on the case of iso-rotation with common angular velocity for crystal and crucible ($\omega_C = \omega_X = 1$), and study the flow and thermal responses in the melt for increasingly higher values of Re, while keeping the thermal Rossby number fixed (and equal to 1.36). We briefly consider some pure buoyancy and counter-rotation cases, as well. For all flat-based crucible simulations, the scaled crystal radius and domain aspect ratio were taken as $r_X = 0.7$, $\Lambda = 0.3$, respectively. These values were also used as a guide to designing the geometry for the curved-based crucibles (described below). For all simulations, the Prandtl number for GaAs (0.068) is applied. A selection of quantitative data obtained for the flat-based crucible cases is shown in Table 2.

4.1 2D/2.5D Simulations

4.1.1 Flat-based crucibles

Simulations were made to study the competing effects of buoyancy and crystal/crucible rotation on the flow and thermal structure and dynamical properties of the melt, starting with flows in cylindrical crucibles. A number of distinctive forms of behaviour were evident, both according to the actual sizes of the Grashof and rotational Reynolds numbers, and their size relative to one another in the scaled system. As an extreme example of the latter, we considered several no-rotation flow problems, with Gr values ranging from 10^3 – 10^7. It was found that for Gr values up to about 10^5, the flow tended to exhibit the same qualitative structure: a single, stationary vortex and a heat-conduction dominated temperature distribution. The latter effect, we note, is common not just here, but for all flows where only a moderate maximum velocity is induced, owing to the large temperature diffusion typical for semiconductor materials. At any point in the domain, the temperature will be significantly advected, only if a strong enough local velocity profile is induced; this implies, in particular, that no significant distortion of the temperature contours will occur below the crystal if the velocity there is too weak, and hence avoids any possible crystal defects due to distorted phase boundaries. This feature is of central importance in our studies. As Gr is raised beyond 10^5, a stronger interplay between the temperature and hydrodynamic fields becomes increasingly more evident, notably beneath the crystal where an undulating pattern for the temperature contours emerges and vortical motion becomes more discernible. This is evident, for example, with the steady flow solution for $Gr = 10^6$ (see Figure 2).

Next simulations were performed with some form of rotation present. The results presented here focus on the case where both crystal and crucible rotate with common angular speed. Very different flow mechanisms are visible, according to whether the directions of rotation are the same (iso-rotation) or opposite (counter-rotation). This difference can perhaps best be illustrated by a couple of examples; for a fixed value of Gr (1.36×10^6), and with $Re = Re_X = 1000$, we consider the crystal having the same rotation rate magnitude, but for iso- and counter-rotation in turn (i.e. $Re_C = \pm Re_X$). Firstly for iso-rotation (Figure 3), we observe a single stationary vortex, diagonally stretched, and with negligible flow beneath the crystal; the azimuthal flow component is non-trivially influenced around where the vortex is located, while the temperature experiences virtually zero feedback from the velocity, and is diffusion-dominated everywhere. In contrast, for counter-rotation (Figure 4), we first note the different flow pattern generated: the vortex, while still stationary, is more horizontally stretched, and significantly, there is stronger motion beneath the crystal; this is perhaps also intuitive, bearing in mind the relatively stronger forces generated, when counter-rotation is produced: we might expect a thin shear layer to emerge in the domain, with rotational speeds varying rapidly from one side to the other: such an effect appears to be evident from the azimuthal flow component plot, in particular. We note moreover, that temperature distortion beneath the crystal is also observable; this again reflects the idea of stronger forces being generated by counter-rotation, leading to stronger localised velocities in certain places (especially beneath the crystal), and a correspondingly more pronounced feedback via advection for the temperature.

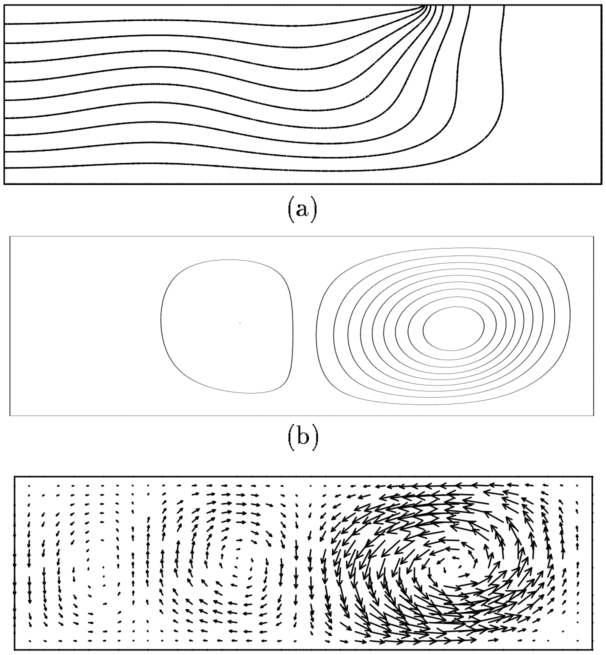

(a)

(b)

(c)

Figure 2: Computed solution for pure buoyancy with $Gr = 10^6$. Results show (a) temperature contours, (b) streamlines (normalised), (c) velocity projection in an arbitrary vertical 'slice'. In (a) the contours range in value from 0 (crystal) to 1 (wall/base) and in (b) from $-1/9$ (left vortex) to 1 (outermost contour of right vortex); the spacing interval is 1/9 in both cases.

4.1.2 Curved-based crucibles

With a particular interest in the growth of semiconductor crystals, we felt it important to try to re-generate the above results, but in a crucible of more 'realistic' design. Based on information obtained from IKZ, we constructed an axisymmetric crucible shape based on polynomial fitting, and used a more realistic temperature distribution on the crucible, based on interpolating some selected data values, again supplied by IKZ. Figure 5 shows the design of our 'realistic' crucible (plus a typical mesh used in our numerical simulations) and can be formally summarised by the alternative definitions of the individual boundary parts:

$$\Gamma_{C_1} := \{(r,z)|r^2 + z^2 - 2zR_O(z_1) = 0 \text{ and } 0 \le r \le 1\}, \tag{4.1a}$$

$$\Gamma_{C_2} := \{(r,z)|r = 1, \text{ and } z_1 \le z \le z_2\}, \tag{4.1b}$$

$$\begin{aligned}\Gamma_B := \{(r,z)|z = z_3 + (r - r_3)^2 \cot(\alpha)/(2(r_3 - r_4)) \text{ and } r_4 \le r \le r_3\}\\ \cup \{(r,z)|z = z_3, \text{ and } r_3 \le r \le 1\},\end{aligned} \tag{4.1c}$$

$$\Gamma_X := \{(r,z)|r^2 + (z - z_5)^2 - 2(z - z_5)R_I(r_4, z_4, z_5) = 0 \text{ and } 0 \le r \le r_4\}. \tag{4.1d}$$

Clearly, the curves Γ_{C_1} and Γ_X define circular arcs and the respective radii are:

$$R_O(z_1) = \frac{(1 + z_1^2)}{2z_1}, \quad R_I(r_4, z_4, z_5) = \frac{r_4^2 + (z_4 - z_5)^2}{2(z_4 - z_5)}. \tag{4.2a,b}$$

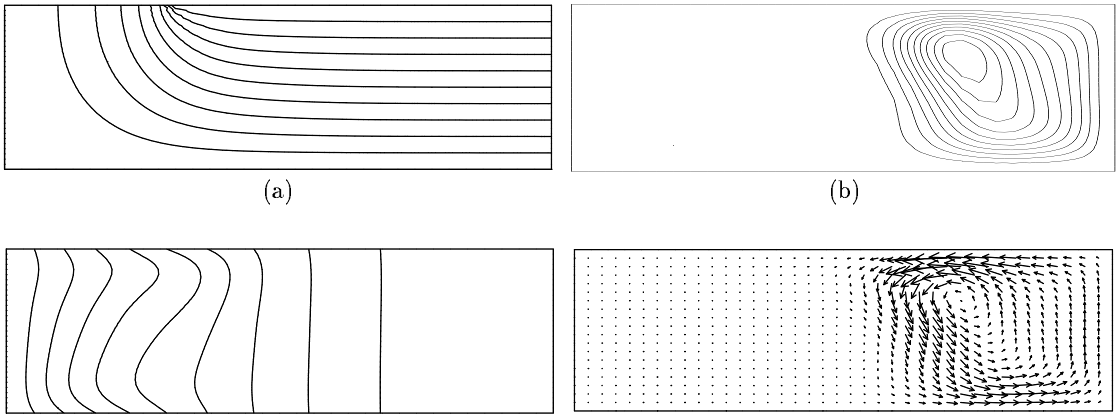

(a) (b)

(c) (d)

Figure 3: Computed solution for iso-rotation with $Re = Re_X = Re_C = 1000$; $Gr = 10^6$. Results show (a) temperature contours, (b) streamlines (normalised), (c) azimuthal velocity component, (d) velocity projection in an arbitrary vertical 'slice'. In (a) the contours range in value from from 0 (crystal) to 1 (wall/base), in (b) from 0.1 (innermost contour) to 1 (outermost contour), and in (c) from 0 (axis) to 1 (wall); the spacing interval is 0.1 in all cases. For (a) and (c), the axis is on the right.

The variables r_3, r_4, z_1 to z_5 and α precisely define the geometry and are indicated in Figure 5. Some restrictions naturally apply, namely, $z_1 \neq 0, r_4 \neq r_3$ and $z_5 \neq z_4$, as well as certain physical limitations, e.g. $z_2 > z_1$. Table 3 shows the values adopted by these variables, as well as temperature data (explained below) in the computations for the results discussed here.

We remark that the parabolic meniscus part of the melt/encapsulant layer shape assumes a contact angle α relative to the negative z-axis, at the melt/encapsulant/crystal annulus of intersection. Secondly, zero gradient is assumed at the lowest point of the curve, i.e. where it meets the straight-portioned part of the boundary. Alternative forms for the parabola have been considered, including using a cubic version, but the results shown here are for the described case above.

The boundary conditions applied are unaltered in form, as compared to (2.5a-c) above, with the exception of the temperature distribution on the crucible. Here, we have replaced the constant-temperature conditions with:

$$T = T_{C_1}(r) \quad \text{on} \quad \Gamma_{C_1}, \tag{4.3a}$$

$$T = T_{C_2}(z) \quad \text{on} \quad \Gamma_{C_2}, \tag{4.3b}$$

where T_{C_1}, T_{C_2} are sufficiently smooth functions, and T is continuous at the junction. Several temperature profiles were considered, including the following two:

$$T_{C_1}(r) = T_0 + \frac{T_1 - T_0}{r_1 - r_0}(r - r_0),\ r \in [0, 1], \tag{4.4a}$$

$$T_{C_2}(z) = T_1 + \frac{T_2 - T_1}{z_2 - z_1}(z - z_1),\ z \in [z_1, z_2]; \tag{4.4b}$$

and

$$T_{C_1}(r) = T_0^{1-r} T_1^r,\ r \in [0, 1], \tag{4.5a}$$

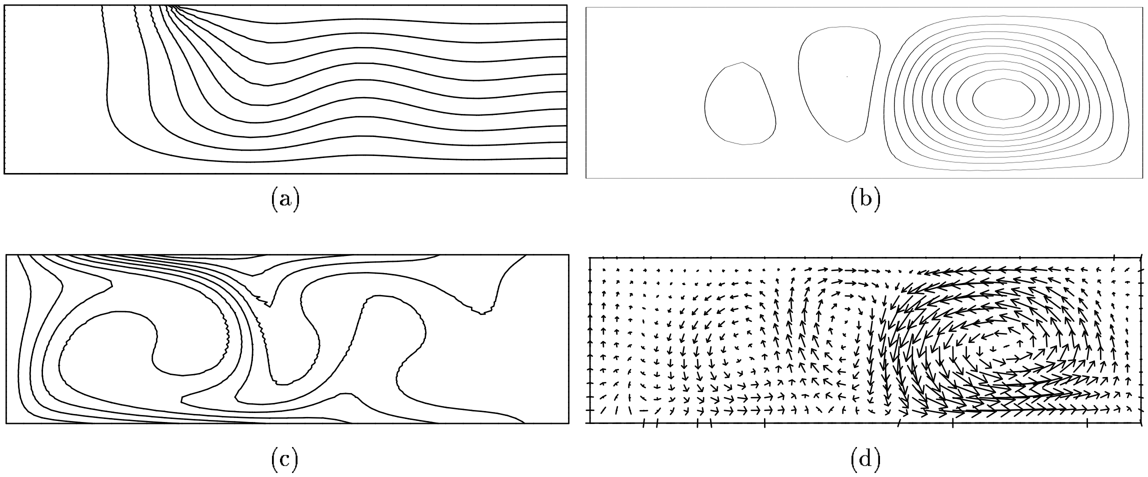

Figure 4: Computed solution for counter-rotation with $Re = Re_X = -Re_C = 1000$; $Gr = 10^6$. Results show (a) temperature contours, (b) streamlines (normalised), (c) azimuthal velocity component, (d) velocity projection in an arbitrary vertical 'slice'. In (a) the contours range in value from from 0 (crystal) to 1 (wall/base), in (b) from $-2/9$ (middle vortex) to 1 (outermost contour of right vortex), and in (c) (viewed along the top) from -1 (wall) to 0.7 (crystal/oxide intersection); the spacing intervals are 0.1, 1/9 and 0.17, respectively. For (a) and (c), the axis is on the right.

$$T_{C_2}(z) = T_1^{\frac{z_2-z}{z_2-z_1}} T_2^{\frac{z-z_1}{z_2-z_1}}, \; z \in [z_1, z_2]. \tag{4.5b}$$

Here T_0, T_1, T_2 denote the temperature values at $(r,z) = (0,0)$, $(r,z) = (1,z_1)$ and $(r,z) = (1,z_2)$, in turn. For the results shown here, the values implemented are given in Table 3.

In an attempt to ascertain the qualitative similarity between flow patterns and thermal distributions arising in flat-based and curved-based cylinders, we ran a series of cases for identical parametric values of Re and Pr; also, we maintained the thermal Rossby number $Gr/Re^2 = 1.36$ throughout. Our results indicate similar qualitative structures with the corresponding 'flat-based' cases, and help to consolidate the relevance of those results. In particular, it was found that for a critical value of the Reynolds number, the flow switches from a steady state to an unsteady state. For $Re = 6365$, Figures 6 and 7 give some indication of the resulting flow behaviour and thermal distribution in the melt, based on using (4.4a,b) and (4.5a,b), respectively – here the time-averaged values in each case are displayed and show good qualitative agreement with the quasi-stationary calculations of Rehse et al (2001). A time-history plot for the former case, indicating the temperature development at the point $(r,z) = (0.18, 0.2)$ lying beneath the crystal/melt interface, is displayed in Figure 8; a frequency analysis has revealed that there is no discernibly dominant frequency here (in contrast to using (4.5a,b), where virtually periodic behaviour occurs for the given Reynolds and Grashof numbers) and tends to suggest the Reynolds number here is significantly larger than the critical value. Subsequent computations with the flat-based geometry suggest a critical value $Re^* \approx 2200$, and we would expect this approximation to be a fair representative for the curved geometry, also.

4.2 3D Simulations

Motivated by the above axisymmetric findings regarding the switch from steady to unsteady motion, a first question was to assess the exact nature of the change of state, allowing for the possible emergence of 3D behaviour. Subsequently, simulations with a full 3D solver were implemented. To simplify the model, we have first reverted to cylindrical geometry, and constant heating of the

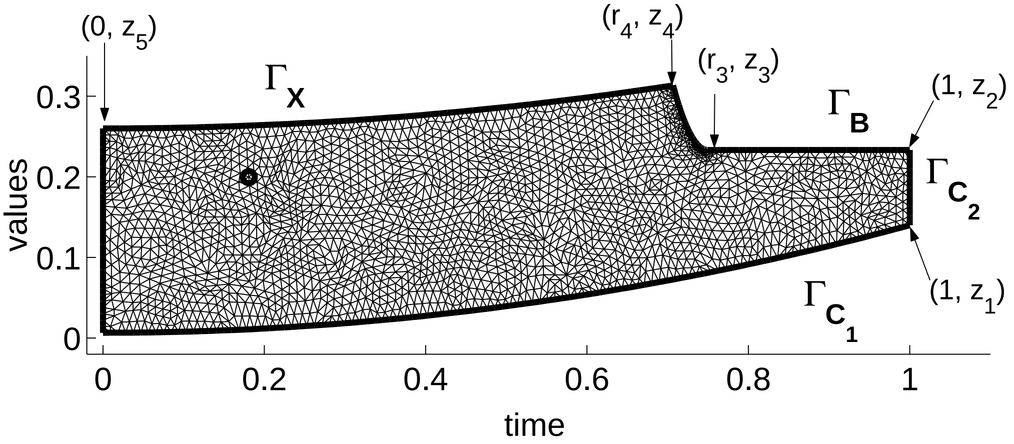

Figure 5: Axisymmetric, curved-based crucible geometry for an arbitrary vertical 'slice'; a typical mesh used for computations is also shown.

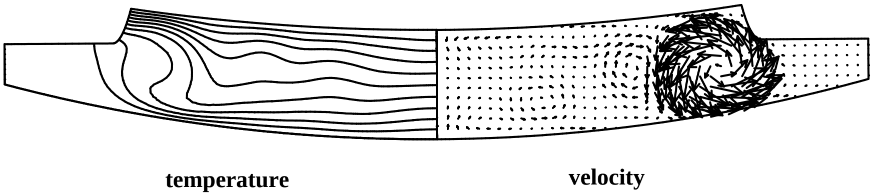

Figure 6: Time-averaged computational solution for iso-rotation with $Re = Re_X = Re_C = 6365$; $Gr = 5.51 \times 10^7$, based on applying $T = 1$ on the crucible. Results show (a) azimuthal velocity component, (b) velocity projection, (c) temperature contours in an arbitrary vertical plane through the axis. The temperature contours range from 0 (crystal) to 1 (wall/base) in intervals of 0.1.

crucible. To help validate the accuracy of the 3D code, a number of analytical flows were first simulated (e.g. simple flow rotation with $\mathbf{u} = r\hat{\mathbf{e}}_\theta$, which is a solution for zero buoyancy and common crystal/crucible angular velocity). Moreover, we made direct quantitative comparisons for sub-critical flows (i.e. flows for which $Re < Re^*$), between the results obtained with the axisymmetric solver and those obtained with the 3D solver. The comparison was generally encouraging, as evidenced for example in Figure 9, where $Re = Re_X = 1700$, $Gr = 3.9304 \times 10^6$. The computed solution is displayed in Figure 10.

Next, we attempted to simulate unsteady flow with the 3D code. In an attempt to gain a better understand of the flow properties around the critical Reynolds number, we have paid particular attention to weakly-supercritical flows (i.e. those satisfying $0 < \epsilon := (Re - Re_*)/Re_* \ll 1$). The subsequent chain of events that occur with such a flow simulation (from an initially two-dimensional state) can perhaps best be illustrated by an example. For this purpose, we consider the case $Re = 2500$ ($Gr = 8.5 \times 10^6$). We refer first to the time-history curve of Figure 11, which shows the difference of successive velocity solutions, as measured by the L_2 norm and applied in the whole domain. The unsteadiness is obviously apparent, but further information is not really forthcoming from this curve alone. However, when we consider local snapshot sequences occurring around certain non-dimensional times, then a more coherent picture forms. It turns out that a very brief two-dimensional phase gives way to a periodic phase, which is already evident from around $t = 20$. Figures 12 ($t = 7.5$) and 13 ($t \approx 150$) illustrate both of these states, and the latter moreover, gives a clear indication that the 3D linear mode with azimuthal wavenumber 4 is dominant at this

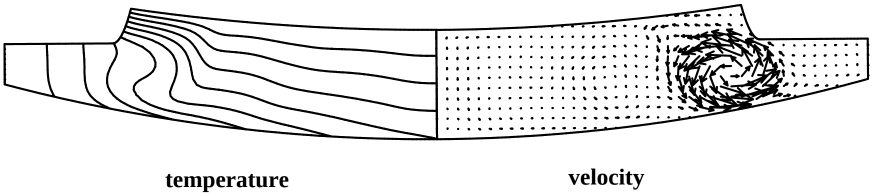

Figure 7: Time-averaged computational solution for iso-rotation with $Re = Re_X = Re_C = 6365$; $Gr = 5.51 \times 10^7$, based on applying the thermal distribution (4.5a,b) on the crucible. Results show (a) azimuthal velocity component, (b) velocity projection, (c) temperature contours in an arbitrary vertical plane through the axis. The temperature contours range from 0 (crystal) to 1 (wall/base intersection) in intervals of 0.1.

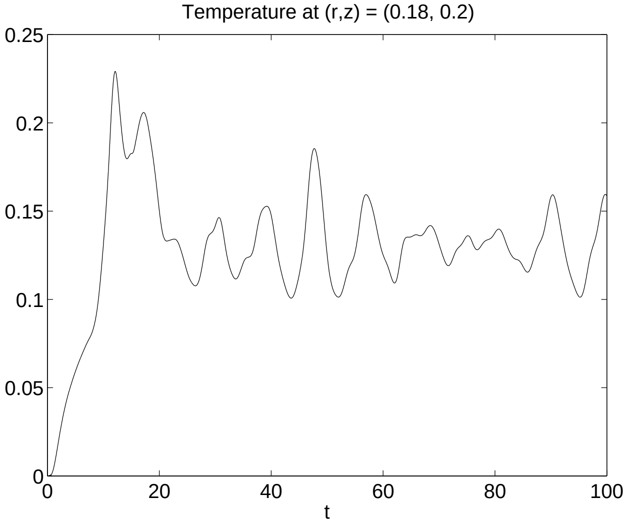

Figure 8: Time-history curve for temperature at the observation point $(r, z) = (0.18, 0.2)$.

stage, owing to the 90° symmetry of the midheight plot. We note moreover, that the flow rotates in an anti-clockwise sense with an approximate period of 18.5 time units. This same periodic state persist until a time of around $t = 350$, when the flow starts to lose this symmetry, eventually becoming fully asymmetric. This is illustrated for $t \approx 535$ in Figure 14. It is noticeable from the '(a)' subplots that the azimuthal velocity component is no longer zero along the axis, and this ties in with the loss of symmetry in the flow solution. We note also that the flow now circulates (still anti-clockwise) with a higher frequency than during the periodic state, having a period here of 12.6 time units, approximately. In terms of instability mode development it is apparent from the symmetric phase that the mode with azimuthal wavenumber 4 is the dominant three-dimensional one. The later loss of symmetry and stronger overall three-dimensionality is consistent with destabilising, weakly-nonlinear modulation of the modes' amplitudes over a relatively slow time scale. A set of curves indicating the behaviour of flow quantities at certain observation points in the domain is given in Figure 15. Here we have defined the Nusselt number on the crystal/melt interface (depicted in Figure 15d) as

$$Nu(t) = \int_{\Gamma_X} \frac{\partial(\mathbf{u} \cdot \hat{\mathbf{e}}_z)}{\partial z}\, ds, \tag{4.6}$$

(s denoting arc length), and this provides a measure for the mean heat transfer from the melt to

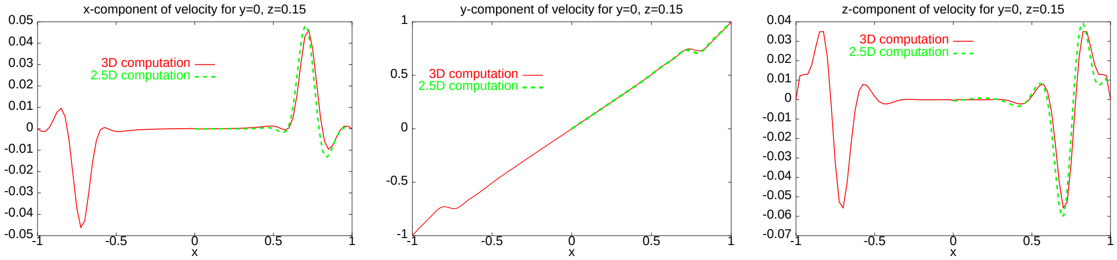

Figure 9: Comparison between results obtained by our axisymmetric and 3D solvers, for the sub-critical case $Re = 1700$; $Gr = 3.93 \times 10^6$, showing (a)radial component, (b) azimuthal component, (c) axial component of velocity in the plane $y = 0$.

the crystal.

In terms of the grown crystal, the time scale for the hydrodynamical effects is considerably larger than that controlling the crystal growth process itself, e.g. the ‘pull speed’ of the crystal is typically of the order of millimetres per hour, which is considerably smaller than the characteristic speed, say, in the melt zone, which has a value more of the order of centimeters per second. This accounts for the fixed-boundary model adopted here, but also demonstrates that, so far as the crystal is concerned, the hydrodynamic time scale is not completely relevant; of more significance is the *time-averaged* melt-flow profile. Figure 16 indicates time-averaged flow profiles (using an ‘end-time’ of t=900). We note here that these profiles are virtually converged, in the sense that no visible alteration in their form is evident for larger times; however, there would be nothing to stop these profiles eventually changing, if the flow were to enter a different phase for a sufficently long time interval, at some later time ($t > 900$). We believe though that the given time-averaged profiles are fairly representative from a qualitative viewpoint. An immediate observation is the significantly-reduced three-dimensional influence; both the velocity and temperature plots reveal only slight three-dimensionality and this feature holds throughout the domain. A second, crucial point is the negligible temperature contour distortion beneath the crystal, clearly visible from Figure 16(c), and which has also been confirmed in other vertical planes containing the axis (not shown). We can conclude therefore that, for the given time interval at least, the time-averaged profiles are pre-dominantly axisymmetric, with very weak temperature advection, and that the three-dimensional effects are operating on shorter time scales.

5 Conclusions and Further Comments

The main focus of this work has been to investigate, under conditions of moderate buoyancy, the influence of crystal and crucible rotation on the flow and thermal fields in the melt zone in vapour-pressure-controlled Czochralski crystal growth. Both axisymmetric and fully three-dimensional simulations have been performed in cylindrical domains, as well as in ‘realistic’ crucibles for the former case.

We first remark on the significantly different qualitative flow patterns found between iso- and counter-rotation of the crucible and crystal. Our results have tended to indicate that for common

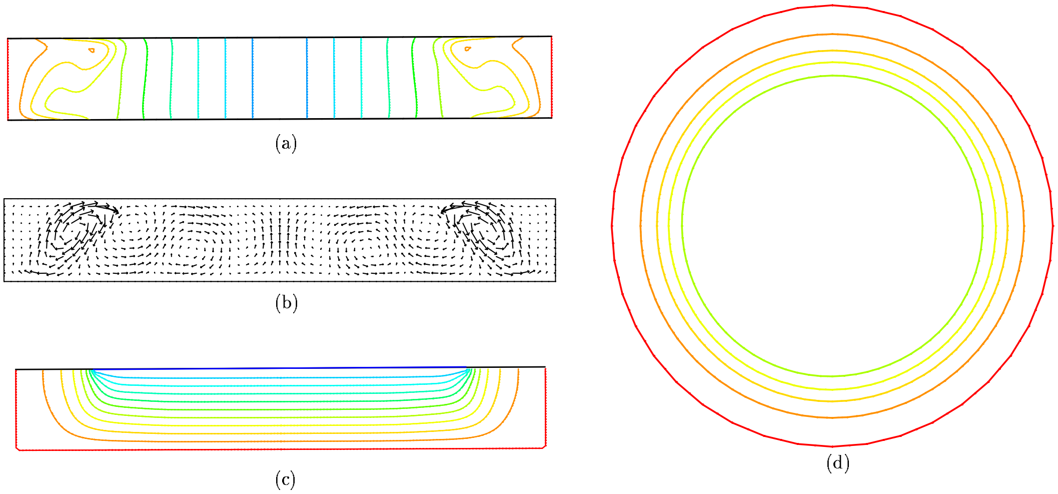

Figure 10: Computed solution for iso-rotation with $Re = Re_X = Re_C = 1700$; $Gr = 3.93 \times 10^6$. Results show (a) azimuthal velocity component, (b) velocity projection, (c) temperature contours, all in the plane $y = 0$, and (d) temperature contours in the midheight plane $z = 0.15$. In (a) the contours range from 0 (axis) to 1 (wall), in (c) from 0 (crystal) to 1 (wall/base), and in (d) inwards from wall (value 1), in each case in intervals of 0.1.

flow parameters the latter effect generally provokes a more widespread flow distribution within the whole domain. The most likely reason for this is the presence of relatively stronger forces within the melt zone; counter-rotation directly induces a thin shear layer in the crucible, within which the angular velocity has to adjust rapidly from one side to the other – the forces generated here are not localised however, and the flow is strongly influenced outside this layer, including (crucially) beneath the crystal. Subsequently, the temperature there is more strongly influenced by advection than in the former case, and moreover, the temperature contours tend to be 'wiggly' beneath the crystal; such an effect is adverse, we note, since it can severely hinder control over the crystal radius, and possible dislocations may not grow outwards. For iso-rotation, in contrast, our simulations have tended to indicate that, for small to moderate Reynolds numbers, the flow is effectively localised as a single vortex towards the crucible wall owing to centrifugal effects, but that the vortex is diagonally stretched, due to the additional influence of buoyancy. Subsequently, weaker temperature distortion is generally observed beneath the crystal. The (steady, axisymmetric) examples for iso- and counter-rotation for $Re = 1000$ given in Section 4 illustrate the aforementioned effects, and more generally we remark that, for all iso-rotation cases tested, where the crystal and crucible have common rotation rates, the temperature profile has been observed to be conduction-dominated throughout the domain for all steady-state flows, including those computed with the curved-based geometry of Section 4.2. It is important however to note here that, despite the apparent advantages of iso-rotation to counter-rotation as mentioned, the former process tends to induce a less homogeneous distribution of dislocations in the crystal, which irreversibly damages parts of the crystal, rendering them useless. Hence, for economical reasons, counter-rotation is often preferred in practice.

Further to the point of steadiness of iso-rotation flows, and viewed from the point of increasing Reynolds number (crystal/crucible rotation rate), the flow is initially steady and axisymmetric until a critical value of Re ($= Re^*$) is attained, at which stage the flow switches to an unsteady state. For the case where the crystal and crucible rotation rates are equal, our computations in a flat cylinder (aspect ratio 0.3) suggest a value $Re^* \approx 2200$, for a fixed thermal Rossby number of 1.36 and Prandtl number 0.068 (GaAs). Three-dimensional results suggest a dominant linear azimuthal mode number of 4, for weakly-supercritical flows; the subsequent loss of symmetry in

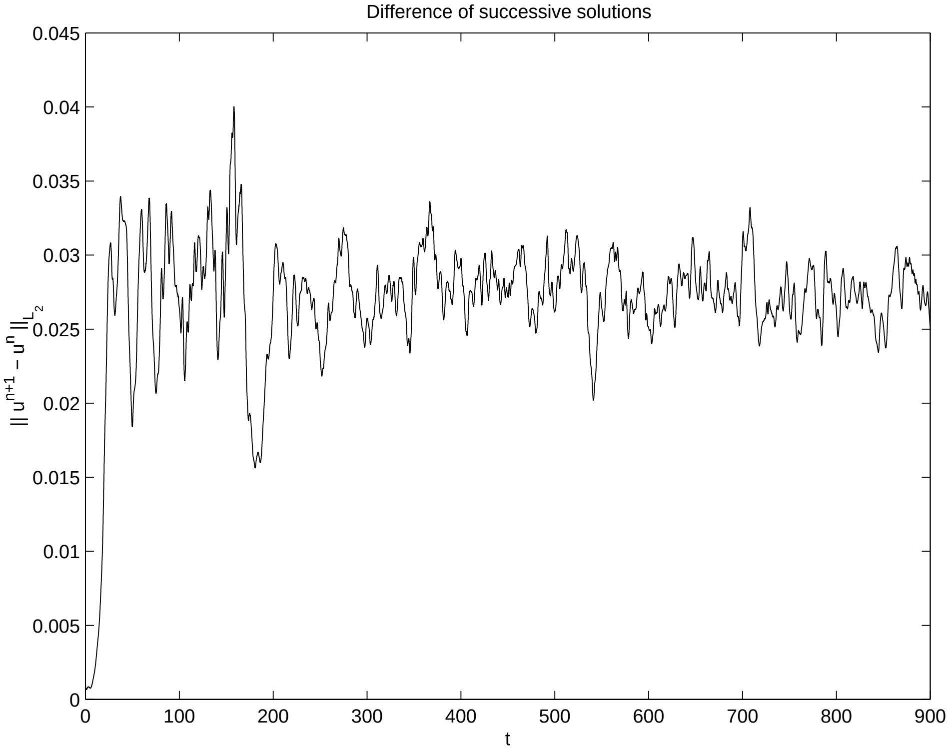

Figure 11: Difference of successive velocity solutions for iso-rotation with $Re = Re_X = Re_C = 2500$; $Gr = 8.5 \times 10^6$. The (stationary, axisymmetric) solution for $Re = 1700, Gr = 3.9304 \times 10^6$ is used as the input solution.

the flow solution at much later times is consistent with the dominant wave amplitude growing nonlinearly on a slow time scale, eventually causing a fully three-dimensional flow to be induced.

Two interesting features arise from the unsteady simulations. Firstly, both axisymmetric and 3D simulations reveal that, while high temperature distortion is evident over the fundamental hydrodynamic time scale, on longer time scales these distortions are mostly cancelled out, leaving only slight wiggles. This feature has been directly observed for Reynolds numbers as high as 6500, albeit mainly from axisymmetric computational results. Secondly, in the 3D simulations the time-averaged solution profiles have been observed to be pre-dominantly two-dimensional. These two features are appropriate to the crystal growth process itself, which develops over a much slower time scale, and suggests that only minimal distortion to the crystallisation front will be induced, leading to approximate convexity there. This is perhaps best demonstrated by the results using the curved-based crucible for $Re = 6365$ (Figures 6,7).

Regarding pure buoyancy, our results have indicated that the flow remains axisymmetric and steady for Grashof numbers up to $Gr = 10^6$ at least, with significant temperature/velocity coupling beneath the crystal first evident from around $Gr = 2 \times 10^5$. As with counter-rotation though, the resulting temperature field distribution there is adverse, i.e. undulating in form. Hence, overall, iso-rotation appears to be most favourable in preserving a wiggle-free temperature field beneath the crystal. This finding, we note, is wholly consistent with the global melt/encapsulant/crystal heat-transfer simulations of Rehse *et al* (2001), although we remark that a quasi-stationary, convection-free model was employed there.

The number of possible parameter regimes is fairly large, and hence, there is a wide range of

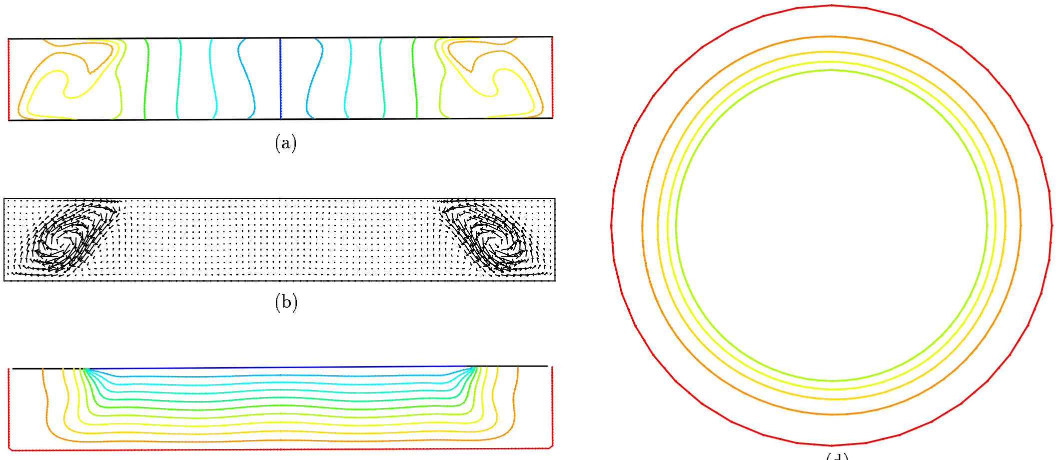

(a)

(b)

(c)

(d)

Figure 12: Snapshots at $t = 7.5$ for iso-rotation with $Re = Re_X = Re_C = 2500$; $Gr = 8.5 \times 10^6$. Results show (a) azimuthal velocity component, (b) velocity projection, (c) temperature contours, all in the plane $y = 0$, and (d) temperature contours in the midheight plane $z = 0.15$. In (a) the contours range from 0 (axis) to 1 (wall), in (c) from 0 (crystal) to 1 (wall/base), and in (d) decrease in value inwards from wall (value 1); the spacing intervals are 0.125, 0.1 and 0.1, respectively.

problems which could be addressed. Until now, we have mostly been concerned with moderate buoyancy; there is clearly scope however to test other cases for different relative sizes of the Grashof and Reynolds numbers, e.g. to analyse the effects of iso- and counter-rotation under stronger conditions of buoyancy (i.e. larger thermal Rossby numbers). Also, iso-rotation with differing rotation rates for crystal and crucible is another area that has not yet been thoroughly investigated by us. Further possibilities include domains of different aspect ratio (Λ) and domains with different crystal radius (r_X).

The model at the phase boundary is naturally simplified here. A follow-up investigation is therefore planned, which will incorporate an appropriate phase-transition model and also allow the position of the crystal/melt interface to move. Typically here we can expect some high temperature gradients across the phase boundary, on account of latent heat release there, and hence, adaptive, fine meshes are likely to be required, owing to the property of globally-continuous temperature for the Taylor–Hood element. Again, axisymmetric and 3D simulations are planned, with the addition of 3D simulations in curved, axisymmetric crucibles with data-interpolated Dirichlet conditions for temperature on the crucible (based on the construction for the 2.5D case, described in Section 4.1 above). A further consideration is the influence of the encapsulant on the melt; it may be more appropriate to replace the present Dirichlet conditions on tangential velocity there, with a continuous shear stress condition, linking the melt and encapsulant flows Such an approach was used for example in Fontaine & Randriamampianina (1989); Fontaine et al (1989); Fontaine, Randriamampianina & Bontoux (1991); as an intermediate step though, it may be beneficial first to implement the non-interactive boundary condition of free shear stress on the interface.

The application of magnetic fields (especially axially directed) has also been a popular recent area in crystal growth generally, since they can help to suppress fluctuations in the melt. In the Czochralski setting, numerical simulations have been made by Hicks, Organ & Riley (1989); Riley (1989); Sabhapathy & Salcudean (1990); Abritska & Gorbunov (1992); Oh & Kang (1996); Talmage et al (2000); Vizman et al (2000) among others.

Acknowledgement

Thanks are due to K. Böttcher, W. Miller and U. Rehse from the Institute for Crystal Growth (IKZ) in Berlin, Germany for the insightful and productive discussions with regard to this work.

References

ABRITSKA, M. YU & GORDUNOV, L. A. 1992 Effect of a variable magnetic field on hydrodynamics of a melt in the process of obtaining monocrystals with Czochralski's method. *Magnetohydrodynamics* **28(4)**, 398–403.

BÄNSCH, E. 1998 Simulation of instationary, incompressible flows. *Acta Math. Univ. Comenianae* **LXVII**, 101–114.

BÄRWOLFF, G. K. F. 1995 Numerical modelling of two- and three-dimensional external and internal unsteady incompressible flow problems. *Computational Fluid Dynamics.* Springer–Verlag, Berlin, Heidelberg, New York, 13–32.

BRISTEAU, M. O., GLOWINSKI, R. & PERIAUX, J. 1987 Numerical methods for the Navier–Stokes equations. Applications to the simulation of compressible and incompressible flows. *Computer Physics Report* **6**, 73–188.

BÜCKLE, U. & SCHÄFER, M. 1993 Benchmark results for the numerical simulation of flow in Czochralski crystal growth. *J. Crystal Growth* **126**, 682–694.

FONTAINE, J. P. & RANDRIAMAMPIANINA, A. 1989 Simulation of flow regimes in a liquid-encapsulated Czochralski configuration. *PhysicoChemical Hydrodynamics* **11(5/6)**, 693–701.

FONTAINE, J. P., RANDRIAMAMPIANINA, A., EXTRÈMET, G. P. & BONTOUX, P. 1989 Simulation of steady and time-dependent rotation-driven regimes in a liquid-encapsulated Czochralski configuration. *J. Crystal Growth* **97**, 116–124.

FONTAINE, J. P., RANDRIAMAMPIANINA, A. & BONTOUX, P. 1991 Numerical simulation of flow structures and instabilities occurring in a liquid-encapsulated Czochralski process. *Phys. Fluids A* **3(10)**, 2310–2331.

GRÄBNER, O., MÜHE, A., MÜLLER, G., TOMZIG, E., VIRBULIS, J. & VON AMMON, W. 2000 Analysis of turbulent flow in silicon melts by optical temperature measurement. *Mater. Sci. Eng. B* **73**, 130–133.

GRESHO, P. M. & SANI, R. L. 2000 *Incompressible flow and the finite element method. Vol. 2: Isothermal laminar flow.* Wiley, Chichester, England.

HICKS, T. W., ORGAN, A. E. & RILEY, N. 1989 Oxygen transport in magnetic Czochralski growth of silicon with a non-uniform magnetic field. *J. Crystal Growth* **94**, 213–228.

MILLER, W. & REHSE, U. 1999 Numerical simulation of temperature and flow field in the melt for the vapour-pressure-controlled Czochralski growth of GaAs. *Crys. Res. Technol.* **36(7)**, 685–694.

MILLER, W., REHSE, U. & BÖTTCHER, K. 1999 Melt convection in a Czochralski crucible. *Crys. Res. Technol.* **34(4)**, 481–489.

OH, H. J. & KANG, I. S. 1999 Effect of crucible geometry on the flow pattern in the magnetic field applied Czochralski process. *J. Crystal Growth* **167**, 345–356.

REHSE, U., MILLER, W., FRANK, CH., RUDOLPH, P. & NEUBERT, M. 1997 A numerical investigation of the effects of iso- and counter-rotation on the shape of the VCz growth interface. *J. Crystal Growth* **230**, 143–147.

RILEY, N. 1989 Species transport in magnetic field Czochralski growth. *J. Crystal Growth* **97**, 76–84.

RUDOLPH, P. & JURICH, M. 1999 Bulk growth of GaAs – an overview. *J. Crystal Growth* **198**, 325–335.

RUDOLPH, P., NEUBERT, M., ARULKUMARAN, S. & SEIFERT, M. 1997 Vapour pressure controlled Czochralski (VCz) growth – a method to produce electronic materials with low dislocation density. Numerical methods for the Navier–Stokes equations. *Crys. Res. Technol.* **32**, 35–50.

SAAD, Y. & SCHULTZ, M. H. 1986 GMRES: A generalised minimal residual algorithm for solving nonsymmetric linear equations. *Siam J. Sci. Stat. Comput.* **7(3)**, 856–869.

SABHAPATHY, P. & SALCUDEAN, M. E. 1990 Numerical study of flow and heat transfer in LEC growth of GaAs with an axial magnetic field. *J. Crystal Growth* **104**, 371–388.

SAVOLAINEN, V., JÄRVINEN, J., RUOKOLAINEN, J. & ANTTILA, O. 2001 A stabilized finite element analysis for three-dimensional Czochralski silicon melt flow. Proceedings of international conference Jyväskylä, Finland, June 28 – July 1, 2000. Tokyo: Gakkotosho. GAKUTO Int. Ser., *Math. Sci. Appl.* **15**, 254-272.

TALMAGE, G., SHYU, S.-H., LOPEZ, J. M. & WALKER, J. S. 2000 Inertial effects in the rotationally driven melt motion during the Czochralski growth of silicon crystals with a strong axial magnetic field. *Z. Angew. Math. Phys.* **51(2)**, 267–289.

VIZMAN, D., FRIEDRICH, J., FISCHER, B. & MÜLLER, G. 2000 3D numerical simulation of melt flow in the presence of a rotating magnetic field. *Int. J. Numer. Methods Heat Fluid Flow* **10(4)**, 366–384.

VIZMAN, D., FRIEDRICH, J. & MÜLLER, G. 2001 Comparison of the predictions from 3D numerical simulation with temperature distributions measured in Si Czochralski melts under the influence of different magnetic fields. *J. Crystal Growth* **230(1–2)**, 73-80.

VIZMAN, D., GRÄBNER, O. & MÜLLER, G. 2001 Three-dimensional numerical simulation of thermal convection in an industrial Czochralski melt. Comparison to experimental results. *J. Crystal Growth* **233(4)**, 687–698.

WATANABE, M., YI, K. W., HIBIYA, T. & KAKIMOTO, K. 1995 Direct observation and numerical simulation of molten silicon flow during crystal growth under magnetic fields by X-ray radiography and large-scale computation *Prog. Crystal Growth Char. Mater.* **38(1-4)** 215–238.

WHEELER, A. A. 1990 Four test problems for the numerical simulation of flow in Czochralski crystal growth. *J. Crystal Growth* **102** 691–695.

Parameter			$(r,z,\theta)=(0.75,0.2,0)$				$r=0, z=0.15$				$(r,z,\theta)=(0.125,0.25,3\pi/4)$				Nusselt no.
Gr	Re_x	Re_c	u_r	u_z	u_θ	T	u_r	u_z	u_θ	T	u_r	u_z	u_θ	T	Nu
10^6	0	0	-0.2023	-0.0235	0	0.7799	0	-0.0706	0	0.4715	-0.0256	-0.0071	0	0.1746	-4.6697
1.36×10^6	10^3	10^3	0.0050	0.0088	0.7842	0.6551	0	0.0007	0	0.5002	0.0002	0.0003	0.1236	0.1670	-4.2757
1.36×10^6	10^3	-10^3	-0.2305	0.0062	-0.4228	0.7905	0	0.0630	0	0.4957	0.0179	0.0007	0.0711	0.1536	-4.7647
3.9304×10^6	1.7×10^3	1.7×10^3	-0.0027	0.0068	0.8003	0.6551	0	-0.0002	0	0.5003	0.0005	0.0001	0.1294	0.1667	-4.4038
8.5×10^6	2.5×10^3	2.5×10^3	0.0117	-0.0023	0.8035	0.6643	0	-0.0017	0	0.4991	-0.0012	-0.0018	0.1267	0.1720	-4.9427

Table 2: Selected quantitative data for each of the flat-based crucible test cases; all cases yield axisymmetric steady motion *except* the last, where the flow is unsteady and 3D – for this case the arithmetic mean value is given for each measurement. The quantities u_r, u_z, u_θ denote the radial, axial and azimuthal velocity components, in turn.

r_3	r_4	z_1	z_2	z_3	z_4	z_5	α	T_0	T_1	T_2
0.7495	0.7067	0.1333	0.2267	0.2267	0.3067	0.2533	15°	0.4	1	0.9

Table 3: Geometric and data values applied to numerical simuations

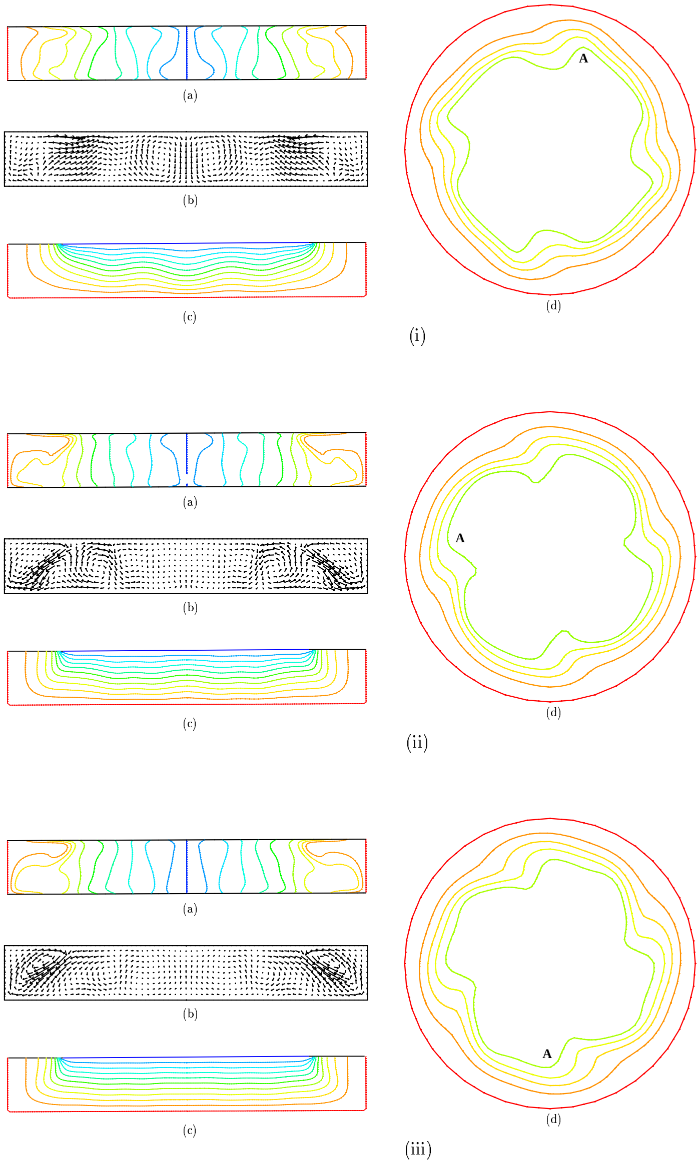

Figure 13: Snapshots at (i) $t = 144$; (ii) $t = 149$; (iii) $t = 154$ for iso-rotation with $Re = Re_X = Re_C = 2500$; $Gr = 8.5 \times 10^6$. For each time, results show (a) azimuthal velocity component, (b) velocity projection, (c) temperature contours, all in the plane $y = 0$, and (d) temperature contours in the midheight plane $z = 0.15$. In (a) the contours range from 0 (axis) to 1 (wall), in (c) from 0 (crystal) to 1 (wall/base), and in (d) decrease in value inwards from wall (value 1), in each case in intervals of 0.1. The point 'A' is used as a marker. (mpeg video at http://www.wias-berlin.de/publications/preprints/852/wias_preprints_852-a.mpg)

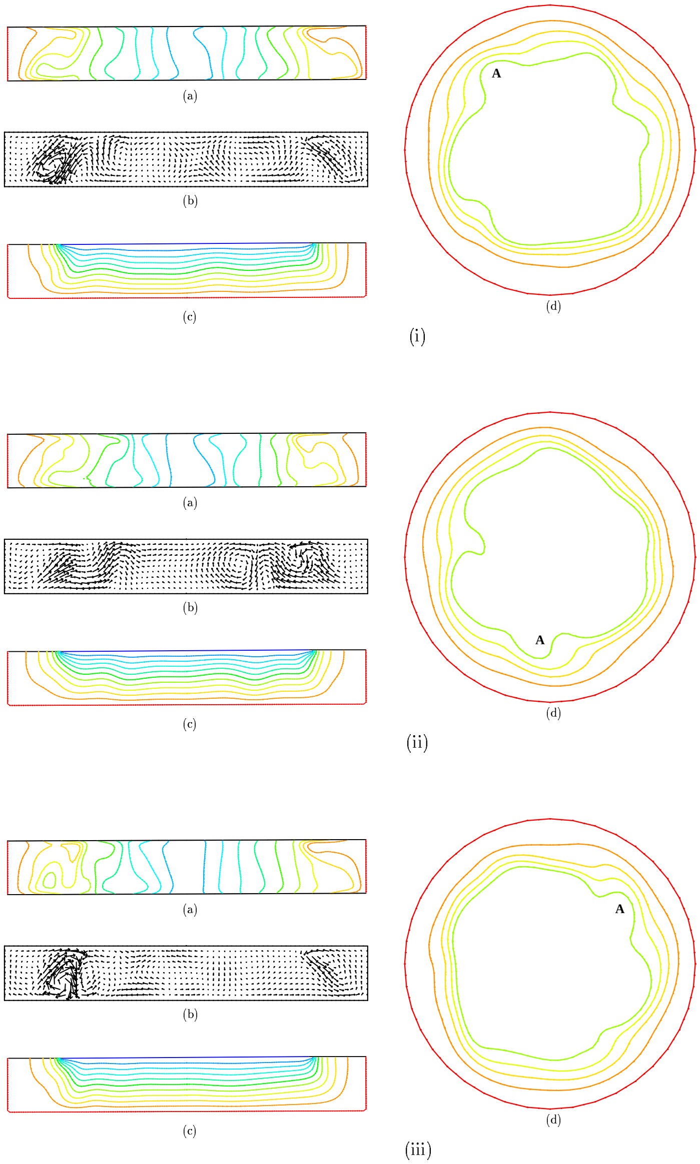

Figure 14: Snapshots at (i) $t = 530$; (ii) $t = 535$; (iii) $t = 540$ for iso-rotation with $Re = Re_X = Re_C = 2500$; $Gr = 8.5 \times 10^6$. For each time, results show (a) azimuthal velocity component, (b) velocity projection, (c) temperature contours, all in the plane $y = 0$, and (d) temperature contours in the midheight plane $z = 0.15$. In (a) the contours decrease in value from 1 (wall), in (c) they range from 0 (crystal) to 1 (wall/base), and in (d) they decrease in value inwards from wall (value 1), in each case in intervals of 0.1. The point 'A' is used as a marker. (mpeg video at http://www.wias-berlin.de/publications/preprints/852/wias_preprints_852-b.mpg)

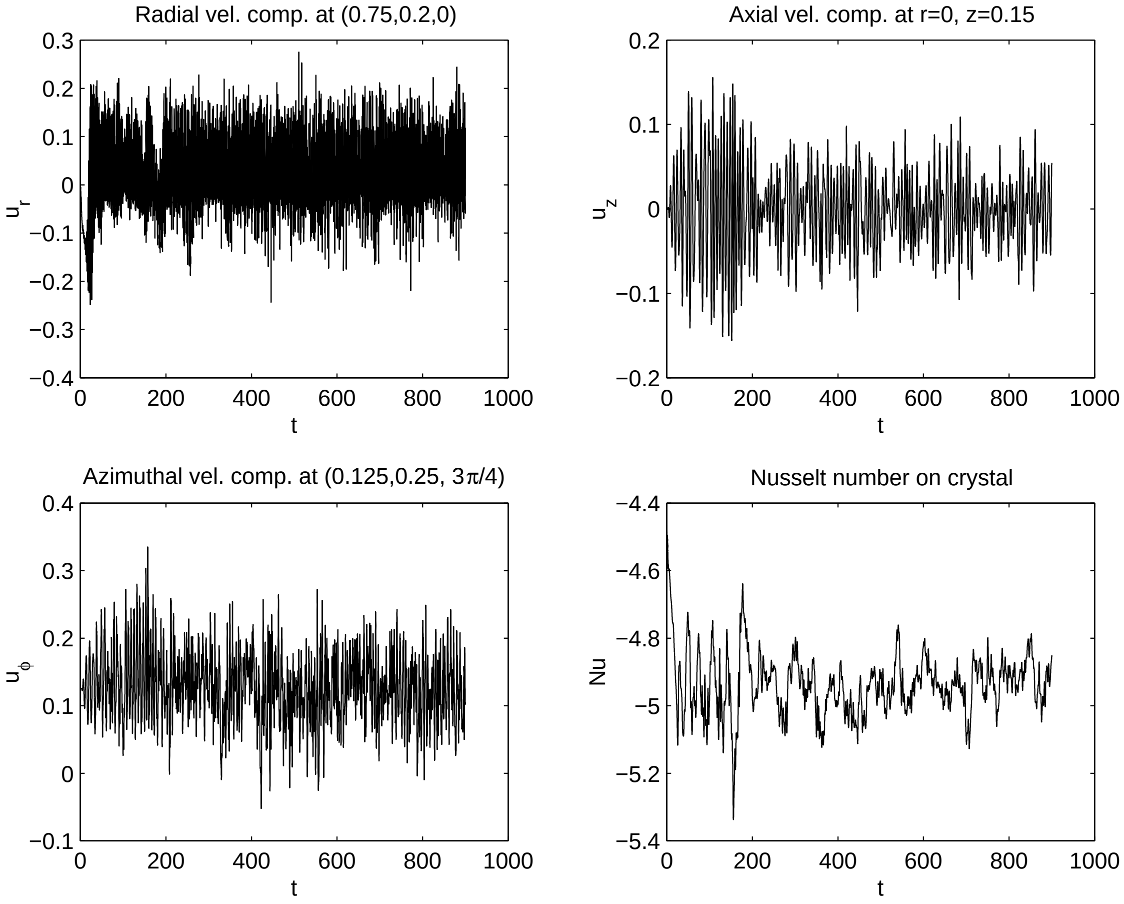

Figure 15: Time-history behaviour of various quantities in a cylindrical crucible with $Re = Re_X = Re_C = 2500; Gr = 8.5 \times 10^6$: upper left – radial velocity component at $r = 0.75, z = 0.2, \theta = 0$; upper right – axial velocity component at $r = 0, z = 0.15$; lower left – azimuthal velocity component at $r = 0.125, z = 0.25, \theta = 3\pi/4$; lower right – Nusselt number on the crystal/melt interface Γ_X.

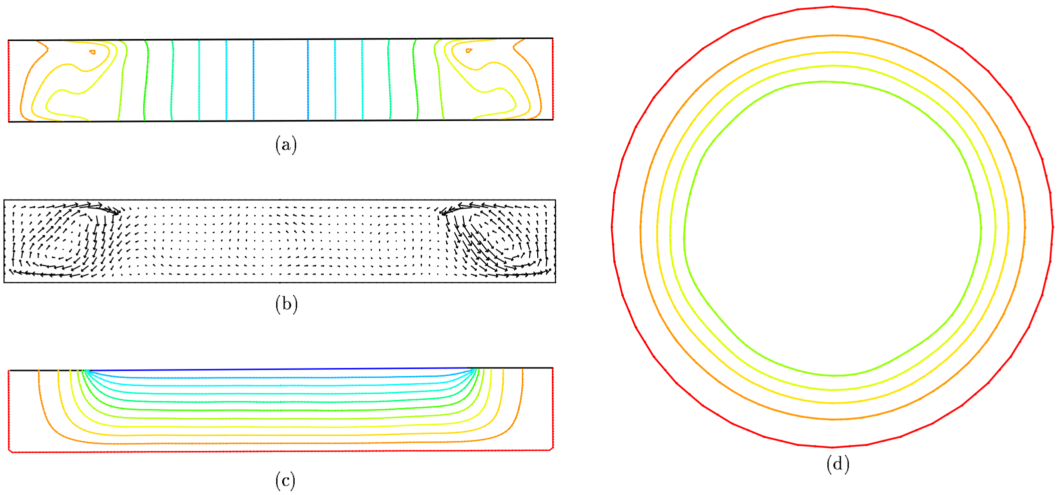

(a)

(b)

(c)

(d)

Figure 16: Time-averaged computational solution for iso-rotation with $Re = Re_X = Re_C = 2500$; $Gr = 8.5\times10^6$. Results show (a) azimuthal velocity component, (b) velocity projection, (c) temperature contours, all in the plane $y = 0$ and (d) temperature contours in the midheight plane $z = 0.15$. In (a) the contours range from 0 (axis) to 1 (wall), in (c) from 0 (crystal) to 1 (wall/base), and in (d) decrease in value inwards from wall (value 1); the spacing intervals are 1/11, 0.1 and 0.1, respectively.